



HAL
open science

Reconstruction of optical inhomogeneities improves fluorescence diffuse optical tomography

Nicolas Ducros, Teresa Correia, Andrea Bassi, Gianluca Valentini, Simon Arridge, Cosimo d'Andrea

► **To cite this version:**

Nicolas Ducros, Teresa Correia, Andrea Bassi, Gianluca Valentini, Simon Arridge, et al.. Reconstruction of optical inhomogeneities improves fluorescence diffuse optical tomography. 2015. hal-01159029v1

HAL Id: hal-01159029

<https://hal.science/hal-01159029v1>

Preprint submitted on 2 Jun 2015 (v1), last revised 18 May 2017 (v4)

HAL is a multi-disciplinary open access archive for the deposit and dissemination of scientific research documents, whether they are published or not. The documents may come from teaching and research institutions in France or abroad, or from public or private research centers.

L'archive ouverte pluridisciplinaire **HAL**, est destinée au dépôt et à la diffusion de documents scientifiques de niveau recherche, publiés ou non, émanant des établissements d'enseignement et de recherche français ou étrangers, des laboratoires publics ou privés.

Reconstruction of optical inhomogeneities improves fluorescence diffuse optical tomography

Nicolas Ducros, Teresa Correia, Andrea Bassi, Gianluca Valentini, Simon Arridge, Cosimo D’Andrea,

Abstract—We propose a new reconstruction algorithm for fluorescence diffuse optical tomography, which is designed for highly heterogeneous objects, such as biological tissues. It is a two-step algorithm that exploits continuous-wave measurements acquired at both excitation and fluorescence wavelengths. First, an optical heterogeneity map, which depends on both absorption and diffusion coefficients, is obtained from excitation measurements. Second, the fluorescence distribution is reconstructed considering the recovered optical heterogeneity map. The algorithm includes dimensionality reduction techniques, namely measurement compression and structured illumination, which significantly reduce acquisition and reconstruction times. The algorithm has been tested on experimental data acquired from tissue-mimicking phantoms considering sparsity priors. We demonstrate the feasibility and effectiveness of this new approach that allows the fluorescence reconstruction quality to be significantly improved with respect to that provided by the standard normalized Born method.

Index Terms—fluorescence imaging, optical tomography, image reconstruction, heterogeneous objects

I. INTRODUCTION

FLUORESCENCE diffuse optical tomography (FDOT), also known as fluorescence molecular tomography (FMT), is an optical technique that allows the 3D reconstruction of the distribution of exogenous fluorescent markers. It has been mainly adopted for *in vivo* preclinical imaging in small animals [1]–[3]. FDOT consists in illuminating a sample with light patterns (e.g. points or more complex shapes) and detecting the fluorescence light exiting the sample [4], [5]. Multiple illumination-detection combinations are generally considered for different angles of view of the sample, which improves the spatial resolution of the reconstruction [6]–[8].

As discussed in [9], tomographic reconstruction of the fluorescent marker distribution generally consists in i) solving the forward problem that describes light propagation through the sample and ii) solving the inverse problem given a forward model. The inverse problem is very ill-posed and thus fluorescence reconstruction highly depends on the accuracy of the forward model itself [10].

N. Ducros is with laboratory CREATIS, INSA-Lyon, CNRS UMR 5220, Inserm U 1044, Université Lyon 1, F-69621 Villeurbanne, France e-mail: (see nicolas.ducros@creatis.insa-lyon.fr).

T. Correia and S. Arridge are with the Centre for Medical Image Computing, University College London, Malet Place, London WC1E 6BT, United Kingdom.

A Bassi, G Valentini, and C D’Andrea are with the Istituto di Fotonica e Nanotecnologie (IFN-CNR) - Dipartimento di Fisica, Politecnico di Milano, Piazza Leonardo da Vinci 32, I-20133 Milan, Italy

C D’Andrea is also with the Center for Nano Science and Technology@PoliMi, Istituto Italiano di Tecnologia, Via Giovanni Pascoli, 70/3, 20133 Milano

The diffusion approximation is generally adopted to solve the forward problem. This partial differential equation, which may be solved by means of the finite element method [11], [12] or the boundary element method [13], [14], requires the knowledge of several optical parameters, principally the absorption coefficient μ_a and reduced scattering coefficient μ'_s at each optical wavelength being measured, as well as the refractive index of the medium, insofar as it affects the determination of correct boundary conditions. One of the major difficulties of FDOT is to estimate the distribution of these optical parameters, which is even more critical when highly heterogeneous objects such as biological samples (e.g. mouse) are considered.

One practical solution has been to assume the sample to be optically homogeneous and consider the ratio between measurements at fluorescence and excitation wavelength. The so-called normalized Born (nBorn) method was originally proposed by Ntziachritos et. al. [15] to correct for experimental factors such as detector gains and coupling losses. Interestingly, it also proved efficient to minimize the fluorescence reconstruction artifacts that appear in the presence of optical inhomogeneities [16]. Although the nBorn approach is effective in the case of absorbing inhomogeneities, it presents severe limitations when scattering inhomogeneities are present [17], [18].

In the last years, FDOT research has focused on multi-modality approaches such as X-ray computed tomography-FDOT (CT-FDOT) [19]–[21], X-ray phase-contrast CT-FDOT [22], magnetic resonance imaging-FDOT (MRI) [23], [24], single photon emission computed tomography-CT-FDOT [25], or positron emission tomography-FDOT [26]. Traditionally, the volume obtained from the concurrent modality, e.g. CT or MRI, is segmented into different anatomical segments, e.g. organs or tissue types. Segments can be used to constrain the solution of the FDOT problems [19]–[22], [27], [28]. As recently demonstrated, knowledge of anatomical segments can improve the reconstruction quality by improving the accuracy of the forward model [17], [29]. This is done by assigning a couple of optical properties to each of the segments [22], [23], [25]. However, choosing the right optical parameters for each segment is very challenging. Despite many studies, the optical properties of the tissues have not yet been fully established, due to inter-subject variability and measurements being predominantly performed using *ex vivo* tissues. Moreover, anatomical information provided by a non-optical concurrent imaging modality is only partially correlated with the optical parameters.

Therefore, it is highly desirable to recover the optical

inhomogeneity maps from optical measurements, which can be done by performing a diffuse optical tomography (DOT) reconstruction at the excitation wavelength. Since continuous wave (CW) measurements at a single wavelength cannot resolve both absorption and scattering coefficients [30], time-resolved/frequency domain or multispectral measurements are required to reconstruct the two inhomogeneity maps. Unfortunately, these two approaches show various drawbacks, such as the complexity of the experimental set-up, a lower signal-to-noise ratio, and huge data sets that are difficult to be managed by the inversion algorithms. In practice, FDOT measurements are often performed in CW mode, especially in the case of a multi-modality instrumentation for which technical constraints push towards the use of simple experimental systems

The authors recently proposed the idea to reconstruct a single optical inhomogeneity map from CW DOT measurements and then to solve the FDOT problem [31]. Capitalizing on this work, we propose a new reconstruction method for FDOT, namely the inhomogeneous nBorn (i-nBorn) method, that generalizes the n-Born method. This new method is based on the joint solution of two inverse problems, which are both ill-posed and require the use of regularization schemes to recover an acceptable solution.

In this contribution, we describe an image reconstruction algorithm for the i-nBorn method. It consists of two main steps. The first step implements a projected Gauss-Newton algorithm, which can accommodate different types of penalty terms, to reconstruct the sample inhomogeneities. The second step, which includes the inhomogeneity map recovered at the first step in the forward model, consists in the fluorescence image reconstruction using anisotropic diffusion (AD) regularization. The algorithm we propose easily integrates the use of structured light illumination and measurement compression, which are dimension reduction approaches that greatly reduce the acquisition and reconstruction times. Structured light is based on the illumination of the object by a small number of light patterns. Patterns can be chosen among natural basis such as Fourier or wavelet [32], using singular value decomposition [29], [33] or applying the compressed sensing paradigm [34]. Measurement compression can be considered as a preprocessing step in which the measured images are (wavelet) compressed and the most significant basis function are retained to build the a forward operator with reduced dimensionality.

The paper is organized as follows. In Section II, we introduce the i-nBorn approach that is designed for fluorescence reconstruction in the presence of optical inhomogeneities. In Section III, we present an overview of our reconstruction method, which is based on the resolution of two inverse problems. First, we introduce dimensionality reduction through measurement compression. Then, we formalize the two inverse problems and explain how we solve them. Next, we describe how to build the forward problems. Finally, we provide a detailed description of our algorithm. In Section IV, we discuss the phantom experiments and the figures of merit of the reconstructions. We present our results in Section V, discuss them in Section VI, and conclude in Section VII.

II. FLUORESCENCE DIFFUSE OPTICAL TOMOGRAPHY IN THE PRESENCE OF INHOMOGENEITIES

We consider an object domain Ω with absorption coefficient $\mu_a(\mathbf{r})$, $\mathbf{r} \in \Omega$, and reduced scattering coefficient $\mu'_s(\mathbf{r})$, $\mathbf{r} \in \Omega$, that has embedded within it a fluorescent dye. Let $h(\mathbf{r})$, $\mathbf{r} \in \Omega$, be the fluorescence yield, which is related to the concentration of the fluorescent dye, then the FDOT image reconstruction problem consists in solving the following inverse problem

$$\Gamma^f = A^f h, \quad (1)$$

where Γ^f is the fluorescence signal measured at the emission wavelength λ^f and A^f is the forward operator. The forward operator A^f strongly depends on the optical properties of the object, which are unknown. The forward operator can be built from estimated optical properties, but the resulting model error can dramatically degrade the reconstruction quality. A practical way of alleviating this problem has been to normalize data, which leads to the normalized FDOT problem

$$\Gamma^n = A^n h, \quad \text{with } \Gamma^n = \frac{\Gamma^f}{\Gamma^x}, \quad (2)$$

where Γ^x is the signal measured at the excitation wavelength λ^x . Unfortunately, this approach does not compensate for the effect of unknown optical inhomogeneities, especially scattering [17], [18]. One possibility is to address the full DOT-FDOT problem for which μ_a , μ'_s and h are all recovered and refractive index is assumed known. It consists in jointly (either sequentially or simultaneously) solving a pair of inverse problems. When the optical properties of the object are assumed to be the same at λ^x and λ^f we have

$$\Gamma^x = F(\mu_a, \mu'_s) \quad \text{and} \quad (3a)$$

$$\Gamma^n = A^n(\mu_a, \mu'_s) h. \quad (3b)$$

where F is the (non-linear) excitation forward model. The pair of maps (μ_a, μ'_s) may be recovered from the DOT problem of Eq. (3a) and then used to build A^n in the FDOT problem of Eq. (3b). However, when CW measurements are considered, the DOT problem has no unique solution [30]. Different pairs of maps (μ_a, μ'_s) may satisfy Eq. (3a), hence the resulting A^n is subject to model error.

In a previous work [31], we suggested an approach that allows DOT-FDOT reconstruction to be performed from CW data. The key idea is to recast the forward problem from a solution to a diffusion equation into a solution of the equivalent Helmholtz equation

$$(\nabla^2 + \eta) \Psi = s \quad (4)$$

where η is a scalar optical property with units of reciprocal squared length, defined as $\eta = \nabla^2(\kappa^{\frac{1}{2}})/\kappa^{\frac{1}{2}} + \mu_a/\kappa$, $\kappa = \frac{1}{3}(\mu'_s + \mu_a)^{-1}$ is the diffusion coefficient inside Ω and Ψ and s are the transformed fluence and source terms. The system of equations (3a)–(3b) may now be rewritten as

$$\Gamma^x = G(\eta), \quad (5a)$$

$$\Gamma^n = B(\eta)\Upsilon, \quad (5b)$$

where Υ is a modified fluorescence yield that is given by

$$\Upsilon = \frac{h}{\kappa}. \quad (6)$$

The strategy to recover h is the following. First, the nonlinear problem of Eq. (5a) is solved and an optical map η , which depends on the optical inhomogeneities of the medium, is obtained. Second, the η map is used to build the forward model B and the linear problem of Eq. (5b) is solved, providing the Υ map. Finally, the unknown fluorescence yield is given by

$$h = \hat{\kappa}\Upsilon, \quad (7)$$

where $\hat{\kappa}$ is chosen, in practice, as an estimate for κ . In this manuscript, we assume κ is slowly varying. Hence, we have the following approximation:

$$\hat{\kappa} \simeq \frac{\hat{\mu}_a}{\eta}, \quad (8)$$

where $\hat{\mu}_a$ is an estimate for the absorption coefficient, chosen as a constant.

III. RECONSTRUCTION OVERVIEW

A. Data Acquisition and Compression

The object Ω is illuminated at I view angles. At each angle, a set of J source patterns is projected onto the object. Such an acquisition results in a set of IJ excitation images and IJ fluorescence images. Let $\mathbf{m}_{i,j}^x$ and $\mathbf{m}_{i,j}^f$ be the excitation and fluorescence images, respectively, measured at the i th view after illumination with the j th source pattern. In the following sections, we use a vector representation for the images, i.e. $\mathbf{m}_{i,j}^x \in \mathbb{R}^P$ and $\mathbf{m}_{i,j}^f \in \mathbb{R}^P$, where P is the number of pixels. The normalized fluorescence image is defined by

$$\mathbf{m}_{i,j}^n = \frac{\mathbf{m}_{i,j}^f}{\mathbf{m}_{i,j}^x}, \quad (9)$$

where the division is component-wise (pixel-wise). Each of the IJ excitation images, as well as each of the IJ normalized fluorescence images, are compressed by applying a wavelet transform \mathbf{D} and retaining their K most relevant wavelet components. The data for each forward problem then consists of the IJK retained components stacked into a vector with components

$$\Gamma_{i,j,k} = \langle \mathbf{d}_{i,j,k}, \mathbf{m}_{i,j} \rangle, \quad (10)$$

where $\mathbf{d}_{i,j,k}^f \in \mathbb{R}^P$ is the wavelet vector associated with the k th component of the image acquired from the j th illumination pattern at the i th angle.

B. Inverse problems

We consider the reconstruction of the unknown quantities $\boldsymbol{\eta} \in \mathbb{R}^N$ and $\mathbf{h} \in \mathbb{R}^N$, where N is the number of voxels, from the measured data $\Gamma^x \in \mathbb{R}^{IJK}$ and $\Gamma^n \in \mathbb{R}^{IJK}$ given the discrete forward models \mathcal{G} and \mathbf{B} . The unknown quantities are obtained minimizing the cost functions

$$\mathcal{L}_{\text{dot}}(\boldsymbol{\eta}) = \frac{1}{2} \|\Gamma^x - \mathcal{G}(\boldsymbol{\eta})\|^2 + \alpha \mathcal{R}_{\text{dot}}(\boldsymbol{\eta}) \quad \text{and} \quad (11a)$$

$$\mathcal{L}_{\text{fdot}}(\boldsymbol{\Upsilon}) = \frac{1}{2} \|\Gamma^n - \mathbf{B}\boldsymbol{\Upsilon}\|^2 + \beta \mathcal{R}_{\text{fdot}}(\boldsymbol{\Upsilon}), \quad (11b)$$

where α (resp. β) is a regularization parameter that sets the trade-off between the data fidelity $\frac{1}{2} \|\Gamma^x - \mathcal{G}(\boldsymbol{\eta})\|^2$ (resp. $\frac{1}{2} \|\Gamma^n - \mathbf{B}\boldsymbol{\Upsilon}\|^2$) and the penalty function \mathcal{R}_{dot} (resp. $\mathcal{R}_{\text{fdot}}$).

Penalty functions have long been confined to ℓ_2 -norm regularization that promotes the smoothness of the solution [19]–[22], [35]. More recently, penalty functions based on ℓ_1 -norm have received a lot of attention, since they promote sparse solutions [26], [36]–[39]. The DOT problem has also been formulated as a joint sparse recovery problem with a ℓ_0 -norm penalty, which assumes that optical heterogeneities have a small support [40].

In the following we present our minimization framework for both \mathcal{L}_{dot} and $\mathcal{L}_{\text{fdot}}$. Remind that $\boldsymbol{\eta}$ is required to build \mathbf{B} , hence, Eq. (11a) has to be solved before Eq. (11b).

1) *Solution of the DOT problem:* The DOT cost function given at Eq. (11a) is minimized using a Gauss-Newton algorithm with a box constrain of the form $\eta_{\min} \leq \eta \leq \eta_{\max}$. The Gauss-Newton method is a traditional tool for non linear minimization, which iteratively solves $\min_{\boldsymbol{\eta}} \mathcal{L}(\boldsymbol{\eta})$ starting with an initial guess $\boldsymbol{\eta}^0$ and building new estimates $\boldsymbol{\eta}^{\ell+1} = \boldsymbol{\eta}^{\ell} + \tau^{\ell} \Delta \boldsymbol{\eta}^{\ell}$, where $\Delta \boldsymbol{\eta}^{\ell}$ is the Gauss-Newton step and τ^{ℓ} is the step length.

$$(\mathbf{J}^{\ell\top} \mathbf{J}^{\ell} + \alpha \mathbf{C}^{\ell}) \Delta \boldsymbol{\eta}^{\ell} = -\mathbf{g}^{\ell}, \quad (12)$$

where \mathbf{J}^{ℓ} is the Jacobian matrix of \mathcal{G} about $\boldsymbol{\eta}^{\ell}$ and \mathbf{C}^{ℓ} is the Hessian matrix of \mathcal{R}_{dot} about $\boldsymbol{\eta}^{\ell}$. The vector \mathbf{g}^{ℓ} , which denotes the gradient of \mathcal{L} at $\boldsymbol{\eta}^{\ell}$, is given by

$$\mathbf{g}^{\ell} = -\mathbf{J}^{\ell\top} (\boldsymbol{\Gamma}^n - \boldsymbol{\mathcal{G}}^{\ell}) + \alpha \nabla \mathcal{R}_{\text{dot}}^{\ell}, \quad (13)$$

where $\boldsymbol{\mathcal{G}}^{\ell} = \mathcal{G}(\boldsymbol{\eta}^{\ell})$ is the forward estimate and $\nabla \mathcal{R}_{\text{dot}}^{\ell}$ is the gradient of \mathcal{R}_{dot} at $\boldsymbol{\eta}^{\ell}$.

Assuming the optical heterogeneity map to be piecewise constant, we choose $\mathcal{R}_{\text{dot}}(\boldsymbol{\eta}) = \text{TV}(\boldsymbol{\eta})$, where TV is the total variation semi-norm. To insure the global convergence of the algorithm, a line search along the direction $\Delta \boldsymbol{\eta}^{\ell}$ is performed, the best step length being retained. Following [41], the box constrain has been implemented determining, at each iteration, a set of fixed variables that are not updated. In the following, we denote $\hat{\boldsymbol{\eta}}$ the solution obtained after convergence of the iterative process.

2) *Solution of the FDOT problem:* The FDOT cost function Eq. (11b) is minimized considering the split operator method introduced in [42], considering a regularization penalty of the form

$$\mathcal{R}_{\text{fdot}}(\boldsymbol{\Upsilon}) = \int_{\Omega} p(|\nabla \mathbf{h}|) \, d\Omega, \quad (14)$$

where p is an edge-preserving potential function. The minimizer of Eq. (11b) is the solution of

$$\mathbf{B}^{\top} (\mathbf{B}\boldsymbol{\Upsilon} - \boldsymbol{\Gamma}^n) = -\beta \mathcal{D}(\boldsymbol{\Upsilon})\boldsymbol{\Upsilon}, \quad (15)$$

where the right-hand side term is the nonlinear anisotropic diffusion with $\mathcal{D}(\boldsymbol{\Upsilon}) = -\nabla \cdot \left[\exp \left[- \left(\frac{|\nabla \boldsymbol{\Upsilon}|}{T} \right)^2 \right] \nabla \right]$, where the parameter T is the threshold [42]–[44]. The solution is obtained using the two-step iterative method described in [42].

C. Forward problems

In this section, we discuss the calculation of the Jacobian matrix \mathbf{J}^{ℓ} , forward estimate $\boldsymbol{\mathcal{G}}^{\ell}$, and weight matrix \mathbf{B} required

in Eq. (12), Eq. (13), and Eq. (15), respectively. All the three quantities require an appropriate model for the propagation of light within the object Ω .

Assuming κ is known on the boundary $\partial\Omega$, we have the following discrete formulation for Eq. (4) using a finite element method (FEM) implementation [11]:

$$\mathbf{H}(\boldsymbol{\eta})\boldsymbol{\Psi} = \mathbf{s} \quad (16)$$

where $\mathbf{H}(\boldsymbol{\eta}) \in \mathbb{R}^{N \times N}$ is the Helmholtz operator that only depends on $\boldsymbol{\eta}$, $\boldsymbol{\Psi} \in \mathbb{R}^{N \times 1}$ is the pseudo photon density vector (which is related to the measured data as detailed in appendix A), and $\mathbf{s} \in \mathbb{R}^{N \times 1}$ is the source vector. The propagation operator has been computed using the Matlab TOAST package [45].

The forward estimate \mathcal{G}^ℓ is of size $IJK \times 1$. The (i, j, k) th entry of \mathcal{G}^ℓ is denoted $\mathcal{G}_{i,j,k}^\ell \in \mathbb{R}$. By definition, it can be computed as

$$\mathcal{G}_{i,j,k}^\ell = \langle \mathbf{d}_{i,j,k}^x, \boldsymbol{\psi}_{i,j}^\ell \rangle \quad (17)$$

where $\boldsymbol{\psi}_{i,j}^\ell$ is obtained solving Eq. (16) with $\mathbf{s} = \mathbf{s}_{i,j}$ at iteration ℓ .

The Jacobian matrix \mathbf{J}^ℓ is of size $IJK \times N$. The (i, j, k) th row of \mathbf{J}^ℓ is denoted $\mathbf{j}_{i,j,k}^\ell \in \mathbb{R}^N$. It may be shown that [9]

$$\mathbf{j}_{i,j,k}^\ell = \boldsymbol{\psi}_{i,j}^\ell \circ \boldsymbol{\psi}_{i,j,k}^\ell, \quad (18)$$

where $\boldsymbol{\psi}_{i,j,k}^\ell$ is the adjoint solution of Eq. (16) for $\mathbf{s} = \mathbf{d}_{i,j,k}^x$ at iteration ℓ . The symbol \circ denotes the Hadamard product.

The weight matrix \mathbf{B} is of size $IJK \times N$. The (i, j, k) th row of \mathbf{B} is denoted $\mathbf{b}_{i,j,k} \in \mathbb{R}^N$. As shown in appendix A, it can be computed as

$$\mathbf{b}_{i,j,k} = \boldsymbol{\psi}_{i,j} \circ \boldsymbol{\psi}_{i,j,k}, \quad (19)$$

where $\boldsymbol{\psi}_{i,j}$ is the solution of Eq. (16) with $\mathbf{s} = \mathbf{s}_{i,j}$ at the final iteration of step 1 while $\boldsymbol{\psi}_{i,j,k}$ is the adjoint solution of Eq. (16) with $\mathbf{s} = \mathbf{d}_{i,j,k}^n / \boldsymbol{\psi}_{i,j}$ (element-wise division).

IV. MATERIAL AND METHODS

A. Experimental set-up

In the following paragraph a brief description of the experimental set-up is reported. A more detailed description can be found in [32], [46]. The light emitted by a diode laser (wavelength of 630 nm, power ≈ 10 mW) is spatially modulated by means of a digital micromirror device (DMD) (Discovery 1100 - ALP1, Vialux), which creates different patterns that are projected onto the sample surface through an objective lens. The sample is placed on a motorized rotational stage in order to acquire multiple views. In particular, measurements have been carried out on biological tissue mimicking phantoms. The light exiting the sample surface is collected by an objective lens ($f = 50$ mm, $f\# = 2.8$, Nikon Co.) and projected on a low noise 16-bit cooled (-40 °C) CCD camera (Versarray 512, Princeton Instruments). In order to discriminate fluorescence from excitation light, a high-pass filter (RG-695, Schott) in conjunction with an interference filter (XF 3076, Omega) have been inserted in front of the objective lens.

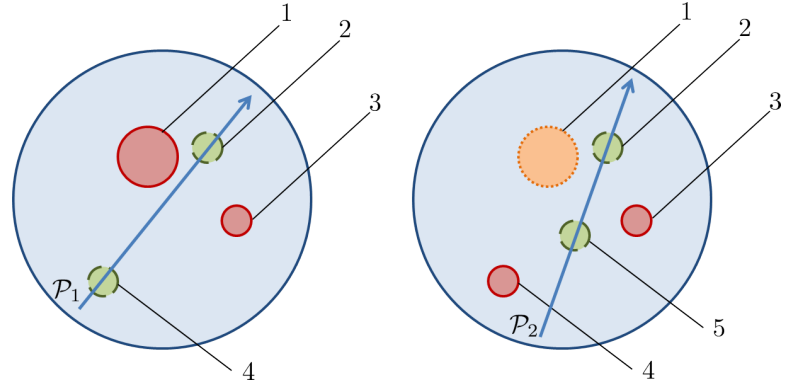


Fig. 1. Top view of the epoxy resin phantoms used in the experiments. Phantom 1 is depicted on the left and phantom 2 on the right. Both phantoms are cylinders of diameter 20 mm and height 80 mm. Red full line (—) indicates absorbing inclusions, green dashed line (---) fluorescence inclusions, and orange dotted line (···) scattering inclusions. The diameter and length of inclusions 1 to 5 are reported in table I. The paths \mathcal{P}_1 and \mathcal{P}_2 are used to plot profiles in figure 6.

| inclusion | 1 | 2 | 3 | 4 | 5 |
|--------------------|----|----|----|----|----|
| \varnothing (mm) | 4 | 2 | 2 | 2 | 2 |
| L (mm) | 30 | 21 | 21 | 30 | 21 |

TABLE I
DIAMETER (\varnothing) AND LENGTH L OF THE HOLES DRILLED INTO THE PHANTOMS.

The phantom is an epoxy resin cylinder of diameter 20 mm and height 80 mm. Appropriate concentrations of toner powder and TiO_2 particles have been added to the resin so as to simulate the absorption and scattering parameters of biological tissues. The optical properties of the phantom have been measured by means of a time-resolved diffused optical spectroscopy system [47]. The following values have been obtained: $\mu_a = 0.02 \text{ mm}^{-1}$ and $\mu'_s = 1.35 \text{ mm}^{-1}$. In order to simulate inclusions, cylindrical holes have been drilled into the phantom at different positions (see figure 1). The diameter and length of the inclusions are reported in table I. Each of the inclusions can be independently filled with a liquid solution whose optical properties differ from the background. In the case of absorbing/scattering inclusions, the solution is made of ink and intralipid® and by changing their concentrations it is possible to modify the absorption and scattering coefficients, respectively. Fluorescent inclusions have been obtained filling the holes with a fluorescent dye (Nile Blue dye concentration of $30 \mu\text{M}$). In particular, two phantoms of increasing complexity have been prepared, as shown in figure 1. In the first phantom, two absorbing cylindrical inclusions (labels 1 and 3 according to figure 1) and two fluorescent inclusions (labels 2 and 4) have been inserted. In the second phantom, two absorbing inclusions (labels 3 and 4), one scattering inclusion (label 1), and two fluorescent inclusions (labels 2 and 5) have been inserted.

Measurements at both excitation and fluorescence wavelengths have been carried out in transmission every 18° , resulting in $I = 20$ views. For simplicity, only $J = 1$ uniform source pattern has been considered at each view angle.

B. Practicalities

The mesh used to solve the Helmholtz-like equation consists of 42886 tetrahedral elements connected by 7468 vertices and is displayed in figure 2a. It was obtained considering the DMD-CCD-based method proposed in [32], which can handle any sample with convex shape without requiring any extra device. Uniform illumination patterns wider than the sample are projected and shadows are recorded rotating the sample with a fine step angle of 1° . The resulting stack of images is filtered backprojected, which results in a 3D volume that is thresholded to get a binary volume indicating the volume in the scene occupied by the sample. Then, the *iso2mesh* mesh generator was employed [48]. The regular reconstruction grid consists of $N = 30 \times 29 \times 59$ voxels of size $(0.75 \text{ mm})^3$. Rectangular illumination and detection areas are determined from a subset of the shadow images primarily measured for determining the shape of the phantom. At each measurement angle (step angle of 20°), the largest rectangle included within the object is retained as the detection area for this particular angle. In order to avoid camera saturation, margins of at least 2 mm are taken from the border of the object. The corresponding illumination area is chosen on the opposite side of the object (see figure 2b). Both illumination area ($34 \text{ mm} \times 17 \text{ mm}$) starts at 2 mm from the top border of the phantom.

The excitation and fluorescence images recorded at each of the $I = 20$ view angles are of size 256×256 (illustrations are provided in figure 2c and 2d). All images are cropped to the detection area and resampled to get rectangular images of $P = 128 \times 64$ pixels. Each of the 20 excitation and 20 fluorescence images are wavelet transformed considering a Daubechies 4 wavelet basis, thanks to the *wavelab* software [49]. For each measured image, $K = 64$ detection patterns are retained among the most significant wavelet basis functions.

C. Performance metrics

The reconstruction quality has been assessed by means of three main objective performance metrics. First, the Pearson correlation has been considered as a global metric that indicates how well two volumes are linearly correlated. Given the ground-truth h^{true} and reconstructed fluorescence distribution h^{rec} , the Pearson correlation ρ is defined by

$$\rho = \frac{\text{cov}(h^{\text{rec}}, h^{\text{true}})}{\sigma(h^{\text{rec}})\sigma(h^{\text{true}})}, \quad (20)$$

where cov is the covariance and σ the standard deviation. A large ρ indicates a high correlation between the images.

Second, the contrast-to-noise ratio (CNR) has been considered. It is defined by

$$C_{\text{roi,back}} = \frac{\mu_{\text{roi}} - \mu_{\text{back}}}{(w_{\text{roi}}\sigma_{\text{roi}}^2 + w_{\text{back}}\sigma_{\text{back}}^2)^{1/2}}, \quad (21)$$

where μ_{roi} (μ_{back}) and σ_{roi} (σ_{back}) are the average and standard deviation of h^{rec} in the region-of-interest Ω_{roi} (background Ω_{back}) and w_{fluo} (w_{back}) is the ratio of the volume occupied by the two fluorescent inclusions (the rest of the volume).

We define the global CNR \mathcal{C} by choosing

$$\Omega_{\text{roi}} = \Omega_A \cup \Omega_B \quad \text{and} \quad \Omega_{\text{back}} = \Omega \setminus \Omega_{\text{roi}}, \quad (22)$$

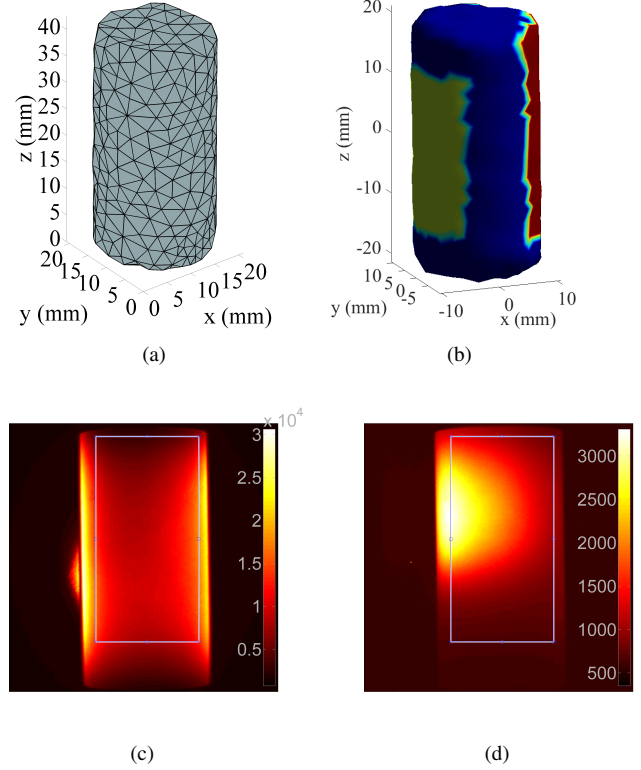


Fig. 2. a) Mesh of the object b) Detection and illumination areas for the first view angle c) image at excitation wavelength d) image at fluorescence wavelength. The rectangles in (c) and (d) indicate the detection area.

where Ω_A (resp. Ω_B) is the support of the first (resp. second) fluorescent inclusion. The larger the CNR, the better.

Last, the relative quantification factor \mathcal{Q} is introduced as a measure of the quantitiveness of the reconstruction. We define

$$\mathcal{Q} = \min\left(\frac{C_A}{C_B}, \frac{C_B}{C_A}\right), \quad (23)$$

where C_A (resp. C_B) is the CNR of inclusion A (resp. B), which is obtained choosing $\Omega_{\text{roi}} = \Omega_A$ (resp. $\Omega_{\text{roi}} = \Omega_B$) and $\Omega_{\text{back}} = \Omega \setminus (\Omega_A \cup \Omega_B)$. The closer the relative quantification is to 1, the better.

D. Choice of the regularization parameters

The reconstruction quality dramatically depends on the choice of the regularization parameters α and β given in Eq. (11a) and Eq. (11b), respectively. While the best α has been chosen from visual inspection, β has been chosen by optimizing an objective performance metric, which enables fair comparisons of the reconstructions. The retained performance metric is the global CNR.

V. RESULTS AND DISCUSSION

The reconstruction of the fluorescence distribution h was performed for the two tissue-mimicking phantoms considering the nBorn method and our proposed approach, setting $\hat{\mu}_a = 0.02 \text{ mm}^{-1}$ and $\hat{\mu}'_s = 1.35 \text{ mm}^{-1}$.

TABLE II
PERFORMANCE METRICS OF THE FLUORESCENCE RECONSTRUCTIONS
CONSIDERING SPARSITY PRIORS, I.E., $\mathcal{R}_{\text{dot}}(\boldsymbol{\eta}) = \text{TV}(\boldsymbol{\eta})$ AND $\mathcal{R}_{\text{fdot}}(\boldsymbol{\Upsilon})$
GIVEN IN EQ. (14)

| Phantom | method | ρ | \mathcal{C} | \mathcal{Q} |
|---------|----------|--------------|---------------|---------------|
| – | perfect | 1 | ∞ | 1 |
| 1 | nBorn | 0.305 | 2.28 | 0.85 |
| 1 | proposed | 0.416 | 3.25 | 0.72 |
| 2 | nBorn | 0.197 | 1.96 | 0.17 |
| 2 | proposed | 0.274 | 2.79 | 0.79 |

TABLE III
PERFORMANCE METRICS OF THE FLUORESCENCE RECONSTRUCTIONS
CONSIDERING REGULARITY PRIORS, I.E., $\mathcal{R}_{\text{dot}}(\boldsymbol{\eta}) = \|\Delta\boldsymbol{\eta}\|_2^2$ AND
 $\mathcal{R}_{\text{fdot}}(\boldsymbol{\Upsilon}) = \|\boldsymbol{\eta}\|_2^2$

| Phantom | method | ρ | \mathcal{C} | \mathcal{Q} |
|---------|----------|--------------|---------------|---------------|
| – | perfect | 1 | ∞ | 1 |
| 1 | nBorn | 0.343 | 2.58 | 0.96 |
| 1 | proposed | 0.424 | 3.31 | 0.95 |
| 2 | nBorn | 0.211 | 2.11 | 0.37 |
| 2 | proposed | 0.235 | 2.36 | 0.87 |

Slices of the heterogeneity maps reconstructed in both phantoms are shown in figure 3. Three-dimensional rendering of the fluorescence reconstructions obtained in phantom 1 and phantom 2 are reported at figure 4 and 5, respectively. To show the universality of our approach, not only the sparsity priors defined in sections III-B1 and III-B2 were considered, but also more classical regularity priors of the form $\mathcal{R}_{\text{dot}}(\boldsymbol{\eta}) = \|\Delta\boldsymbol{\eta}\|_2^2$ and $\mathcal{R}_{\text{fdot}}(\boldsymbol{\Upsilon}) = \|\boldsymbol{\eta}\|_2^2$ [19]–[22], [35]. For both phantom reconstructions, the fluorescence profiles obtained along paths \mathcal{P}_1 and \mathcal{P}_2 (refer to figure 1 to localize the paths) are depicted in figure 6 considering sparsity priors as well as regularity priors. Finally, the performance metrics introduced in section IV-C were used to evaluate both phantoms reconstructions considering the standard nBorn approach and our proposed approach. The metrics are reported in table II for reconstructions performed with sparsity priors and in table III for reconstructions performed with regularity priors.

In the reconstructed fluorescence volume obtained from phantom 1, we observe a clear advantage of the proposed approach with respect to the standard nBorn method as can be observed visually in the 3D rendering of figure 4 and in the profiles of the top row of figure 6. In particular, the nBorn reconstruction is unable to resolve separately the two inclusions as our proposed approach does. This is quantitatively confirmed with the increase of the global CNR of the reconstructed volume \mathcal{C} and its correlation with the ground truth ρ (see table II and table III). Specifically, we observe a 36 % increase (resp. 23 %) of ρ and a 42 % increase (resp. 28 %) of \mathcal{C} for the sparsity (resp. smooth) priors. Improvements are obtained for both prior types, which suggests the i-nBorn method outperforms the standard nBorn method regardless the penalty functional chosen for regularization. A small decrease of 15 % (resp. 1 %) of the relative quantification \mathcal{Q} is observed in phantom 1 with sparsity (resp. smooth) priors.

In the second phantom, similar results are obtained. As

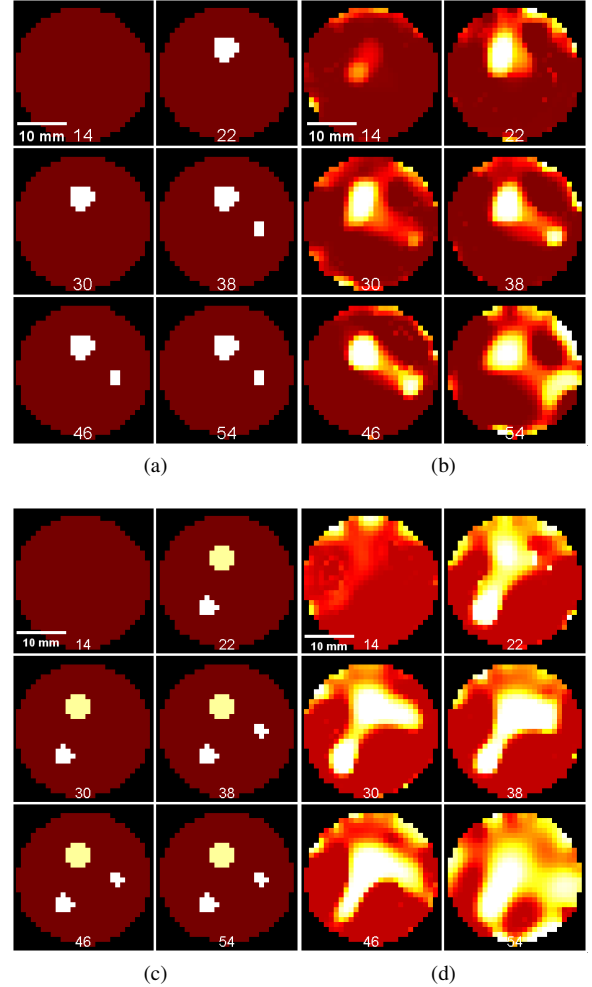


Fig. 3. Optical inhomogeneity maps. a) ground truth in phantom 1, b) reconstruction in phantom 1, c) ground truth in phantom 2, b) reconstruction in phantom 2.

shown in figure 5 and in the bottom row of figure 6, the two fluorescent inclusions cannot be separated considering nBorn-based reconstruction while they can be well discriminated and localized by means of the proposed method. Specifically, we observe a 39 % increase (resp. 11 %) of ρ and a 42 % increase (resp. 12 %) of \mathcal{C} for the sparsity (resp. smooth) priors. The advantage of the proposed method is even more evident due to the higher complexity of the absorbing/scattering inhomogeneities distribution. Beyond the higher number of inhomogeneities and their variability –both absorbing and scattering inclusions are present, the distance between the two fluorescent inclusions is smaller in phantom 2 than in phantom 1 (see figure 1). For this phantom, we observe a dramatic increase of the relative quantification \mathcal{Q} , which is increased by a factor of 3.7 for sparsity priors and by a factor of 1.37 for smooth priors.

Finally, we remark that the relative quantification is much better in phantom 1 than in phantom 2 when the standard nBorn method is considered while the proposed i-nBorn algorithm tends to provide similar quantification capabilities whatever the complexity of the phantom and the priors used

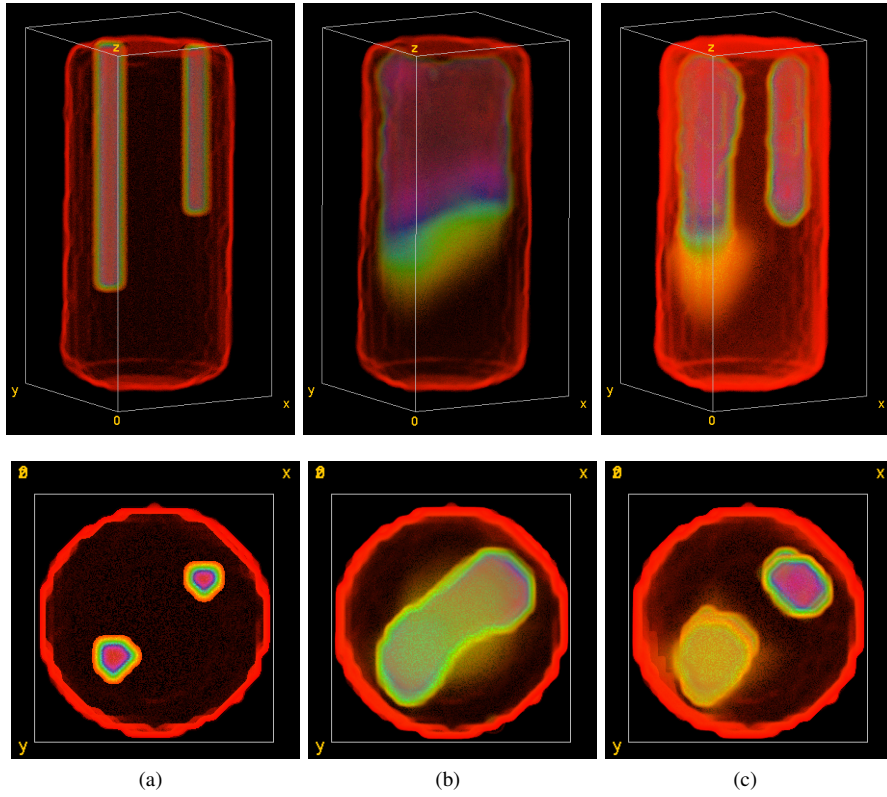


Fig. 4. Fluorescence reconstructions in phantom 1. a) ground truth, b) standard nBorn reconstruction, c) reconstruction obtained with the proposed i-nBorn algorithm.

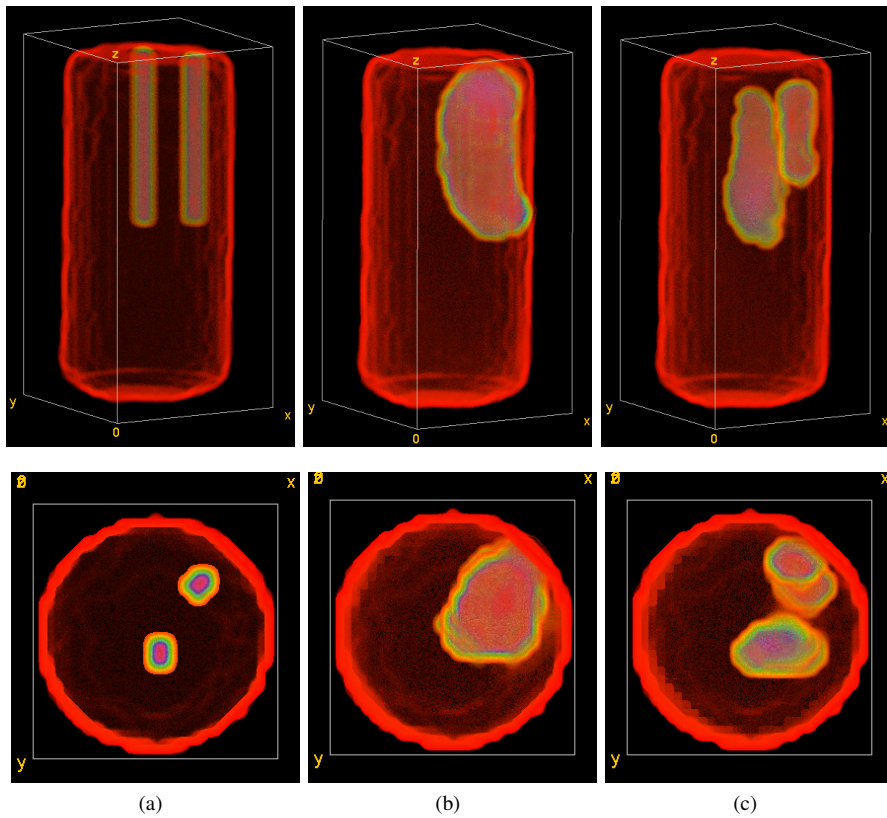


Fig. 5. Fluorescence reconstructions in phantom 2. a) ground truth, b) standard nBorn reconstruction, c) reconstruction obtained with the proposed i-nBorn algorithm.

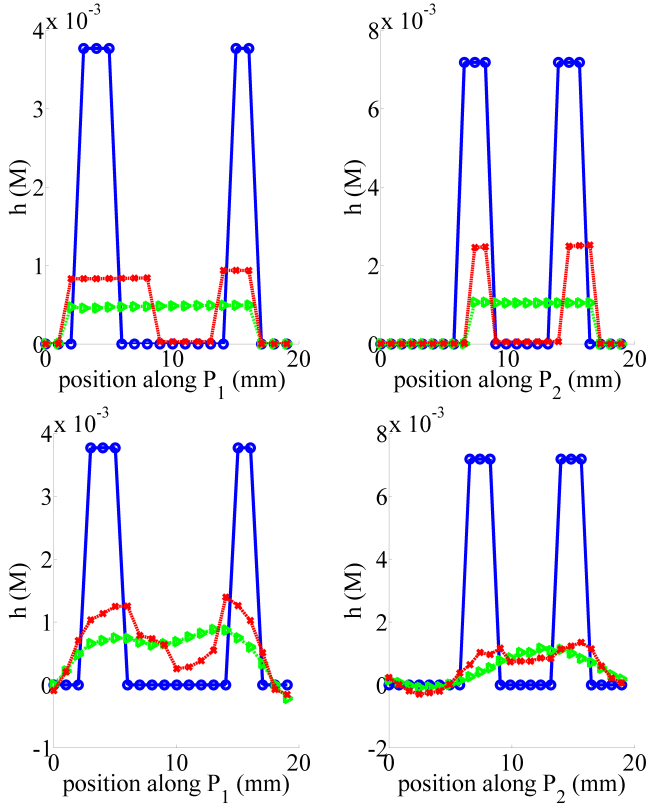


Fig. 6. Reconstructed fluorescence profiles considering the nBorn approach (green line marked with \triangleright) and our method (red line marked with \times). The phantom profiles are provided for comparison (blue solid line marked with \circ). Left column, profiles are plotted along path \mathcal{P}_1 . Right column, path \mathcal{P}_2 is considered. Top row, the sparsity priors $\mathcal{R}_{\text{dot}}(\boldsymbol{\eta}) = \text{TV}(\boldsymbol{\eta})$ and $\mathcal{R}_{\text{fdot}}$ given in Eq. (14) are considered. Bottom row, the smooth priors $\mathcal{R}_{\text{dot}}(\boldsymbol{\eta}) = \|\Delta\boldsymbol{\eta}\|_2^2$ and $\mathcal{R}_{\text{fdot}}(\boldsymbol{\Upsilon}) = \|\boldsymbol{\eta}\|_2^2$ are chosen. For each of the four cases, the reconstructed fluorescence distributions have been normalized to a unit marker quantity such that $\int h(\mathbf{r}) d\Omega = 1 \mu\text{mol}$.

in the reconstruction algorithm.

VI. DISCUSSION

Our approach represents a simple and effective way to experimentally capture the optical inhomogeneities needed to accurately model light propagation within biological tissues. We demonstrated that an optical inhomogeneity map can be recovered from CW measurements in tissue mimicking phantoms. Even without discriminating absorbing from scattering inclusions, the proposed method proved efficient to improve the quality of the fluorescence reconstructions. In particular, an increase of the CNR and correlation of the reconstruction with the ground truth is observed in all our measurements. The dramatic loss of quantification capabilities, which has already been reported elsewhere for the nBorn approach in the presence of complex phantoms [17], can be alleviated considering our approach. This could be a fundamental step towards applications such as follow-up studies in oncology.

These results demonstrate the importance to incorporate the optical inhomogeneities into the forward model involved in FDOT reconstructions. They confirm that the nBorn method only partially compensates the fluorescence reconstruction errors due to the presence of optical heterogeneities, especially

in the presence of scattering inclusions [17]. The advantage of the proposed i-nBorn algorithm is particularly evident in the case of phantom 2 that contains both absorbing and scattering inhomogeneities as well as close fluorescent inclusions. It is worth noting that also in the simpler phantom 1, the nBorn method is outperformed by our approach. We anticipate that the advantage of the proposed approach over the standard nBorn method would be even stronger if an anatomical prior obtained by a concurrent anatomical modality is available.

The i-nBorn method can be understood as a generalisation of the standard nBorn method. Indeed, the i-nBorn method is equivalent to the nBorn method for homogeneous samples. The nBorn method provides a preliminary fluorescence reconstruction that can be improved by reconstructing the optical inhomogeneities of the sample. It is worth reminding that the two advantages offered by the nBorn normalization, namely independence to experimental gains and optical inhomogeneity compensation, are preserved by the i-nBorn method.

Finally, it is worth mentioning that the possibility to localize absorbing and/or scattering inclusions by means of CW measurements, even without discriminating between them, is of great interest for different applications based on optical contrast, e.g. optical oxymetry [50] and mammography [51]. In particular, the proposed method can be exploited to localize anomalous inhomogeneities and then more complex (e.g. time-resolved) measurements schemes can be used to discriminate between absorbing and scattering inclusions and quantify the two optical parameters.

VII. CONCLUSION

In this paper, we demonstrated the feasibility and advantage of a novel FDOT reconstruction algorithm, which is designed for highly heterogeneous samples. By reconstructing an optical inhomogeneity map from CW measurements, it is possible to improve the fluorescence reconstruction quality. We believe that the so-called i-nBorn method together with the proposed algorithm can be of particular interest in combination with non-optical techniques, such as MRI and CT. In such a multimodal scheme, the non-optical modality would provide high resolution *a priori* about the localization of the optical inhomogeneities, while DOT measurements could provide an *in situ* optical characterization of the inhomogeneities. The combination of both types of optical information could be a fundamental step towards improved 3D resolution and quantification of fluorescence markers *in vivo*.

APPENDIX A

PROOF OF THE WEIGHT MATRIX FORMULA

The pseudo photon density ψ obeys the following coupled equations [31]:

$$\mathcal{H}\psi^x = s \text{ in } \Omega \quad (24a)$$

$$\mathcal{H}\psi^f = \psi^x \Upsilon \text{ in } \Omega. \quad (24b)$$

where \mathcal{H} is the Helmholtz operator with Robin boundary conditions on $\partial\Omega$. The optical properties are assumed to be the same at both excitation and fluorescence wavelengths.

Let Σ be the portion of object surface viewed by the camera. Measurements are obtained from the photon density by means of the $\mathbb{R}(\Omega) \rightarrow \mathbb{R}(\Sigma)$ measurement operator \mathcal{M} . We have

$$m = \mathcal{M}\psi. \quad (25)$$

Any compressed measurement Γ^n is the projection of the uncompressed measurement m^n onto some detection pattern d . We have:

$$\Gamma^n = \langle m^n, d \rangle_{\Sigma} \quad (26)$$

where $\langle \cdot, \cdot \rangle_{\Sigma}$ denotes the L^2 -inner product, i.e. $\langle f, g \rangle_{\Sigma} = \int_{\Sigma} f(\mathbf{x})g(\mathbf{x}) dx$. By definition of m^n , we have

$$m = \left\langle \frac{m^f}{m^x}, d \right\rangle_{\Sigma} \quad (27)$$

Using Eq. (25), we have

$$m = \left\langle \frac{\mathcal{M}\psi^f}{\mathcal{M}\psi^x}, d \right\rangle_{\Sigma} \quad (28)$$

$$= \left\langle \mathcal{M}\psi^f, \frac{d}{\mathcal{M}\psi^x} \right\rangle_{\Sigma}. \quad (29)$$

Introducing the Green's operator of the Helmholtz Eqs. (24) leads to

$$m = \left\langle \mathcal{M}\mathcal{G}^f[\psi^x\Upsilon], \frac{d}{\mathcal{M}\psi^x} \right\rangle_{\Sigma}. \quad (30)$$

By definition of the adjoint operator \mathcal{G}^{f*} , we have:

$$= \left\langle \psi^x\Upsilon, \mathcal{G}^{f*}\mathcal{M}^* \left[\frac{d}{\mathcal{M}\psi^x} \right] \right\rangle_{\Omega} \quad (31)$$

Isolating Υ that is the quantity of interest, we obtain

$$m = \left\langle \psi^x\mathcal{G}^{f*}\mathcal{M}^* \left[\frac{d}{\mathcal{M}\psi^x} \right], \Upsilon \right\rangle_{\Omega} \quad (32)$$

The operator \mathcal{G}^f being self adjoint, we obtain

$$m = \left\langle \psi^x\mathcal{G}^f\mathcal{M}^* \left[\frac{d}{\mathcal{M}\psi^x} \right], \Upsilon \right\rangle_{\Omega} \quad (33)$$

In practice, a measurement may be modelled as

$$\mathcal{M}\psi = f(\mathbf{r})\psi(\mathbf{r}), \quad \forall \mathbf{r} \in \Sigma \quad (34)$$

where $f \in \mathbb{R}(\Sigma)$ depends on the optical properties, the geometry of acquisition and some gain factors. By definition of the adjoint operator that satisfies $\langle \mathcal{M}\psi, m \rangle_{\Sigma} = \langle \psi, \mathcal{M}^*m \rangle_{\Omega}$, $\forall \psi \in \mathbb{R}(\Omega)$, $m \in \mathbb{R}(\Sigma)$, we have

$$\mathcal{M}^*m = \begin{cases} f(\mathbf{r})m(\mathbf{r}), & \forall \mathbf{r} \in \Sigma \\ 0 & \forall \mathbf{r} \in \Omega \setminus \Sigma \end{cases} \quad (35)$$

Inserting Eq. (34) and Eq. (35) into Eq. (33) leads to :

$$m = \left\langle \psi^x\mathcal{G}^f \left[\frac{d|_{\Omega}}{\psi^x} \right], \Upsilon \right\rangle_{\Omega} \quad (36)$$

where $d|_{\Omega} = d$ for $\mathbf{r} \in \Sigma$ and 0 for $\mathbf{r} \in \Omega \setminus \Sigma$. Discretizing the previous equation completes the proof.

ACKNOWLEDGMENT

The research leading to these results has received funding from LASERLAB-EUROPE (grant agreement no. 284464, EC's Seventh Framework Programme)

REFERENCES

- [1] S. R. Cherry, "In vivo molecular and genomic imaging: new challenges for imaging physics," *Physics in Medicine and Biology*, vol. 49, pp. R13–R48, 2004.
- [2] V. Ntziachristos, C. Bremer, and R. Weissleder, "Fluorescence imaging with near-infrared light: new technological advances that enable in vivo molecular imaging," *European radiology*, vol. 13, no. 1, pp. 195–208, Jan. 2003. [Online]. Available: <http://www.ncbi.nlm.nih.gov/pubmed/12541130>
- [3] F. Stuker, J. Ripoll, and M. Rudin, "Fluorescence molecular tomography: Principles and potential for pharmaceutical research," *Pharmaceutics*, vol. 3, no. 2, pp. 229–274, Apr. 2011. [Online]. Available: <http://www.mdpi.com/1999-4923/3/2/229/>
- [4] J. Chen, V. Venugopal, F. Lesage, and X. Intes, "Time-resolved diffuse optical tomography with patterned-light illumination and detection," *Opt. Lett.*, vol. 35, no. 13, pp. 2121–2123, Jul 2010. [Online]. Available: <http://ol.osa.org/abstract.cfm?URI=ol-35-13-2121>
- [5] N. Ducros, C. D'andrea, G. Valentini, T. Rudge, S. Arridge, and A. Bassi, "Full-wavelet approach for fluorescence diffuse optical tomography with structured illumination," *Opt. Lett.*, vol. 35, no. 21, pp. 3676–3678, 2010. [Online]. Available: <http://ol.osa.org/abstract.cfm?URI=ol-35-21-3676>
- [6] G. Zacharakis, J. Ripoll, R. Weissleder, and V. Ntziachristos, "Fluorescent protein tomography scanner for small animal imaging," *IEEE Transactions on Medical Imaging*, vol. 24, no. 7, pp. 878–885, 2005. [Online]. Available: [GotoISI://000230218800007](http://dx.doi.org/10.1109/TMI.2005.8540007)
- [7] T. Lasser, A. Soubret, J. Ripoll, and V. Ntziachristos, "Surface reconstruction for free-space 360 fluorescence molecular tomography and the effects of animal motion," *Medical Imaging, IEEE Transactions on*, vol. 27, no. 2, pp. 188–194, Feb. 2008.
- [8] N. Ducros, A. Bassi, G. Valentini, M. Schweiger, S. Arridge, and C. D'Andrea, "Multiple-view fluorescence optical tomography reconstruction using compression of experimental data," *Opt. Lett.*, vol. 36, no. 8, pp. 1377–1379, Apr 2011. [Online]. Available: <http://ol.osa.org/abstract.cfm?URI=ol-36-8-1377>
- [9] S. R. Arridge and J. C. Schotland, "Optical tomography: forward and inverse problems," *Inverse Problems*, vol. 25, no. 12, p. 123010 (59pp), 2009. [Online]. Available: <http://stacks.iop.org/0266-5611/25/123010>
- [10] M. Mozumder, T. Tarvainen, S. Arridge, J. P. Kaipio, C. d'Andrea, and V. Kolehmainen, "Approximate marginalization of absorption and scattering in fluorescence diffuse optical tomography," *submitted*, 2015. [Online]. Available: <http://arxiv.org/abs/1501.00384>
- [11] M. Schweiger, S. R. Arridge, M. Hiraoka, and D. T. Delpy, "The finite element method for the propagation of light in scattering media: Boundary and source conditions," *Medical Physics*, vol. 22, no. 11, pp. 1779–1792, 1995. [Online]. Available: <http://link.aip.org/link/?MPH/22/1779/1>
- [12] M. Guven, L. Zhou, L. Reilly-Raska, and B. Yazici, "Discretization error analysis and adaptive meshing algorithms for fluorescence diffuse optical tomography: Part ii," *Medical Imaging, IEEE Transactions on*, vol. 29, no. 2, pp. 230–245, feb. 2010.
- [13] T. Gzywacz, J. Sikora, and S. Wojtowicz, "Substructuring methods for 3-d bem multilayered model for diffuse optical tomography problems," *Magnetics, IEEE Transactions on*, vol. 44, no. 6, pp. 1374–1377, June 2008.
- [14] J. Elisee, A. Gibson, and S. Arridge, "Combination of boundary element method and finite element method in diffuse optical tomography," *Biomedical Engineering, IEEE Transactions on*, vol. 57, no. 11, pp. 2737–2745, Nov 2010.
- [15] V. Ntziachristos and R. Weissleder, "Experimental three-dimensional fluorescence reconstruction of diffuse media by use of a normalized Born approximation," *Opt. Lett.*, vol. 26, no. 12, pp. 893–895, 2001. [Online]. Available: <http://ol.osa.org/abstract.cfm?URI=ol-26-12-893>
- [16] A. Soubret, J. Ripoll, and V. Ntziachristos, "Accuracy of fluorescent tomography in the presence of heterogeneities: Study of the normalized Born ratio," *Ieee Transactions on Medical Imaging*, vol. 24, no. 10, pp. 1377–1386, 2005. [Online]. Available: [GotoISI://000232236800013](http://dx.doi.org/10.1109/TMI.2005.8540013)

- [17] T. Pyka, R. Schulz, A. Ale, and V. Ntziachristos, "Revisiting the normalized Born approximation: effects of scattering," *Opt. Lett.*, vol. 36, no. 22, pp. 4329–4331, Nov 2011. [Online]. Available: <http://ol.osa.org/abstract.cfm?URI=ol-36-22-4329>
- [18] J. F. P.-J. Abascal, J. Aguirre, J. Chamorro-Servent, M. Schweiger, S. Arridge, J. Ripoll, J. J. Vaquero, and M. Desco, "Influence of absorption and scattering on the quantification of fluorescence diffuse optical tomography using normalized data," *Journal of Biomedical Optics*, vol. 17, no. 3, pp. 036 013–1–036 013–9, 2012. [Online]. Available: [+http://dx.doi.org/10.1117/1.JBO.17.3.036013](http://dx.doi.org/10.1117/1.JBO.17.3.036013)
- [19] R. Schulz, A. Ale, A. Sarantopoulos, M. Freyer, E. Soehngen, M. Zientkowska, and V. Ntziachristos, "Hybrid system for simultaneous fluorescence and x-ray computed tomography," *IEEE Transactions on Medical Imaging*, vol. 29, no. 2, pp. 465–473, 2010.
- [20] X. Guo, X. Liu, A. Wang, F. Tian, F. Liu, B. Zhang, G. Hu, and J. Bai, "A combined fluorescence and microcomputed tomography system for small animal imaging," *Biomedical Engineering, IEEE Transactions on*, vol. 57, no. 12, pp. 2876–2883, Dec 2010.
- [21] X. Liu, X. Guo, F. Liu, Y. Zhang, H. Zhang, G. Hu, and J. Bai, "Imaging of indocyanine green perfusion in mouse liver with fluorescence diffuse optical tomography," *Biomedical Engineering, IEEE Transactions on*, vol. 58, no. 8, pp. 2139–2143, Aug 2011.
- [22] P. Mohajerani, A. Hipp, M. Willner, M. Marschner, M. Trajkovic-Arsic, X. Ma, N. Burton, U. Klemm, K. Radrich, V. Ermolayev, S. Tzoumas, J. Siveke, M. Bech, F. Pfeiffer, and V. Ntziachristos, "Fmt-pcct: Hybrid fluorescence molecular tomography—x-ray phase-contrast ct imaging of mouse models," *Medical Imaging, IEEE Transactions on*, vol. 33, no. 7, pp. 1434–1446, July 2014.
- [23] X. Zhang, V. Y. Toronov, and A. G. Webb, "Integrated measurement system for simultaneous functional magnetic resonance imaging and diffuse optical tomography in human brain mapping," *Review of Scientific Instruments*, vol. 77, no. 11, pp. 114 301–114 301–8, Nov 2006.
- [24] F. Stuker, C. Baltes, K. Dikaïou, D. Vats, L. Carrara, E. Charbon, J. Ripoll, and M. Rudin, "Hybrid small animal imaging system combining magnetic resonance imaging with fluorescence tomography using single photon avalanche diode detectors," *IEEE Transactions on Medical Imaging*, vol. 30, no. 6, pp. 1265–1273, 2011.
- [25] M. Solomon, R. E. Nothdruff, W. Akers, W. B. Edwards, K. Liang, B. Xu, G. P. Suddlow, H. Deghani, Y.-C. Tai, A. T. Eggebrecht, S. Achilefu, and J. P. Culver, "Multimodal fluorescence-mediated tomography and spect/ct for small-animal imaging," *Journal of nuclear medicine : official publication, Society of Nuclear Medicine*, vol. 54, no. 4, pp. 639–46, Apr. 2013. [Online]. Available: <http://www.ncbi.nlm.nih.gov/pubmed/23447655>
- [26] B. Zhang, S. Liu, X. Cao, F. Liu, X. Wang, J. Luo, B. Shan, and J. Bai, "Fluorescence tomography reconstruction with simultaneous positron emission tomography priors," *Multimedia, IEEE Transactions on*, vol. 15, no. 5, pp. 1031–1038, Aug 2013.
- [27] J.-C. Baritaux, K. Hassler, and M. Unser, "An efficient numerical method for general l_p regularization in fluorescence molecular tomography," *Medical Imaging, IEEE Transactions on*, vol. 29, no. 4, pp. 1075–1087, april 2010.
- [28] J.-C. Baritaux, K. Hassler, M. Bucher, S. Sanyal, and M. Unser, "Sparsity-driven reconstruction for fdot with anatomical priors," *Medical Imaging, IEEE Transactions on*, vol. 30, no. 5, pp. 1143–1153, may 2011.
- [29] P. Mohajerani and V. Ntziachristos, "Compression of Born ratio for fluorescence molecular tomography / X-ray computed tomography hybrid imaging : methodology and in vivo validation," *Opt. Lett.*, vol. 38, no. 13, pp. 2324–2326, 2013.
- [30] S. R. Arridge and W. R. B. Lionheart, "Nonuniqueness in diffusion-based optical tomography," *Opt. Lett.*, vol. 23, no. 11, pp. 882–884, 1998. [Online]. Available: <http://ol.osa.org/abstract.cfm?URI=ol-23-11-882>
- [31] T. Correia, N. Ducros, C. D'Andrea, M. Schweiger, and S. Arridge, "Quantitative fluorescence diffuse optical tomography in the presence of heterogeneities," *Opt. Lett.*, vol. 38, no. 11, pp. 1903–1905, Jun 2013. [Online]. Available: <http://ol.osa.org/abstract.cfm?URI=ol-38-11-1903>
- [32] N. Ducros, A. Bassi, G. Valentini, G. Canti, S. Arridge, and C. D'Andrea, "Fluorescence molecular tomography of an animal model using structured light rotating view acquisition," *Journal of Biomedical Optics*, vol. 18, no. 2, pp. 020 503–020 503, 2013. [Online]. Available: [+http://dx.doi.org/10.1117/1.JBO.18.2.020503](http://dx.doi.org/10.1117/1.JBO.18.2.020503)
- [33] D. Wang, X. Liu, F. Liu, and J. Bai, "Full-angle fluorescence diffuse optical tomography with spatially coded parallel excitation," *Information Technology in Biomedicine, IEEE Transactions on*, vol. 14, no. 6, pp. 1346–1354, Nov 2010.
- [34] A. Jin, B. Yazici, and V. Ntziachristos, "Light illumination and detection patterns for fluorescence diffuse optical tomography based on compressive sensing," *Image Processing, IEEE Transactions on*, vol. 23, no. 6, pp. 2609–2624, June 2014.
- [35] D. Hyde, E. Miller, D. Brooks, and V. Ntziachristos, "Data specific spatially varying regularization for multimodal fluorescence molecular tomography," *Medical Imaging, IEEE Transactions on*, vol. 29, no. 2, pp. 365–374, feb. 2010.
- [36] X. Cao, B. Zhang, F. Liu, X. Wang, and J. Bai, "Reconstruction for limited-projection fluorescence molecular tomography based on projected restarted conjugate gradient normal residual," *Opt. Lett.*, vol. 36, no. 23, pp. 4515–4517, Dec 2011. [Online]. Available: <http://ol.osa.org/abstract.cfm?URI=ol-36-23-4515>
- [37] C. B. Shaw and P. K. Yalavarthy, "Effective contrast recovery in rapid dynamic near-infrared diffuse optical tomography using 1-norm-based linear image reconstruction method," *Journal of Biomedical Optics*, vol. 17, no. 8, pp. 086 009–086 009, 2012. [Online]. Available: <http://dx.doi.org/10.1117/1.JBO.17.8.086009>
- [38] J. Prakash, H. Dehghani, B. Pogue, and P. Yalavarthy, "Model-resolution-based basis pursuit deconvolution improves diffuse optical tomographic imaging," *Medical Imaging, IEEE Transactions on*, vol. 33, no. 4, pp. 891–901, April 2014.
- [39] J. Prakash, C. Shaw, R. Manjappa, R. Kanhiroan, and P. Yalavarthy, "Sparse recovery methods hold promise for diffuse optical tomographic image reconstruction," *Selected Topics in Quantum Electronics, IEEE Journal of*, vol. 20, no. 2, pp. 74–82, March 2014.
- [40] O. K. Lee, J. M. Kim, Y. Bresler, and J. C. Ye, "Compressive diffuse optical tomography: Noniterative exact reconstruction using joint sparsity," *Medical Imaging, IEEE Transactions on*, vol. 30, no. 5, pp. 1129–1142, May 2011.
- [41] D. Kim, S. Sra, and I. Dhillon, "Tackling box-constrained optimization via a new projected quasi-newton approach," *SIAM Journal on Scientific Computing*, vol. 32, no. 6, pp. 3548–3563, 2010. [Online]. Available: <http://epubs.siam.org/doi/abs/10.1137/08073812X>
- [42] T. Correia, J. Aguirre, A. Sisniega, J. Chamorro-Servent, J. Abascal, J. J. Vaquero, M. Desco, V. Kolehmainen, and S. Arridge, "Split operator method for fluorescence diffuse optical tomography using anisotropic diffusion regularisation with prior anatomical information," *Biomed. Opt. Express*, vol. 2, no. 9, pp. 2632–2648, Sep 2011. [Online]. Available: <http://www.opticsinfobase.org/boe/abstract.cfm?URI=boe-2-9-2632>
- [43] M. Black, G. Sapiro, D. Marimont, and D. Heeger, "Robust anisotropic diffusion," *Image Processing, IEEE Transactions on*, vol. 7, no. 3, pp. 421–432, Mar 1998.
- [44] A. Douiri, M. Schweiger, J. Riley, and S. R. Arridge, "Anisotropic diffusion regularization methods for diffuse optical tomography using edge prior information," *Measurement Science and Technology*, vol. 18, no. 1, p. 87, 2007. [Online]. Available: <http://stacks.iop.org/0957-0233/18/i=1/a=011>
- [45] M. Schweiger and S. Arridge, "The toast++ software suite for forward and inverse modeling in optical tomography," *Journal of biomedical optics*, vol. 19, no. 4, p. 040801, Apr. 2014. [Online]. Available: <http://www.ncbi.nlm.nih.gov/pubmed/24781586>
- [46] N. Ducros, C. D'Andrea, A. Bassi, G. Valentini, and S. Arridge, "A virtual source pattern method for fluorescence tomography with structured light," *Physics in Medicine and Biology*, vol. 57, no. 12, p. 3811, 2012. [Online]. Available: <http://stacks.iop.org/0031-9155/57/i=12/a=3811>
- [47] A. Bassi, A. Farina, C. D'Andrea, A. Pifferi, G. Valentini, and R. C. ., "Portable, large-bandwidth time-resolved system for diffuse optical spectroscopy," *Opt. Express*, vol. 15, no. 22, p. 1448214487., 2007.
- [48] Q. Fang and D. Boas, "Tetrahedral mesh generation from volumetric binary and grayscale images," in *Biomedical Imaging: From Nano to Macro, 2009. ISBI '09. IEEE International Symposium on*, June 2009, pp. 1142–1145.
- [49] [Online]. Available: <http://statweb.stanford.edu/~wavelab/>
- [50] M. Ferrari and V. Quaresima, "A brief review on the history of human functional near-infrared spectroscopy (fNIRS) development and fields of application," *NeuroImage*, vol. 63, no. 2, pp. 921–35, Nov. 2012. [Online]. Available: <http://www.ncbi.nlm.nih.gov/pubmed/22510258>
- [51] A. Pifferi, A. Farina, A. Torricelli, G. Quarto, R. Cubeddu, and P. Taroni, "Review: Time-domain broadband near infrared spectroscopy of the female breast: a focused review from basic principles to future perspectives," *J. Near Infrared Spectrosc.*, vol. 20, no. 223, 2012.